TITLE

Stem cells partner with matrix remodeling cells during regeneration

AUTHORS

Blair W. Benham-Pyle[1,2,3,4,#], Frederick G. Mann Jr.[1,2,#], Carolyn E. Brewster[1], Enya R. Dewars[1], Stephanie H. Nowotarski[1,2], Carlos Guerrero-Hernández[1], Seth Malloy[1], Kate E. Hall[1], Lucinda E. Maddera[1], Shiyuan Chen[1], Jason A. Morrison[1], Brian D. Slaughter[1], Anoja Perera[1], Alejandro Sánchez Alvarado[1,2,*]

[#]These authors contributed equally. Author order was determined by coin flip.
*Correspondence should be addressed to Alejandro Sánchez Alvarado.

Affiliations

1. Stowers Institute for Medical Research, Kansas City, MO, USA
2. Howard Hughes Institute for Medical Research, Kansas City, MO, USA
3. Stem Cells and Regenerative Medicine Center, Cell and Gene Therapy Center, Baylor College of Medicine, Houston, TX, USA
4. Department of Molecular and Cellular Biology, Baylor College of Medicine, Houston TX USA

SUMMARY

Regeneration of missing or damaged tissue requires the concerted activities of both pre-existing and newly generated cells. While previous studies identified regeneration-induced gene expression programs in tissues and single cells[1–6], emerging spatial transcriptomic methods can place these programs into their organismal context at near cellular resolution[7–11]. Here we report a spatial transcriptomic atlas of whole-body regeneration and identify changes in gene expression patterning and tissue architecture during regeneration. We produced spatially resolved RNA-seq data from regenerating tail fragments of the free-living planarian *Schmidtea mediterranea*. Comparison of fragments 6 and 48 hours after amputation revealed time-dependent changes in gene expression patterns and cellular associations. Notable examples include re-localization of *agat-1*$^{+}$ epidermal cells from lateral edges to both lateral and anterior edges and the discovery of wound-induced association of stem cells with cells expressing the matrix remodeling gene *matrix metalloproteinase-1*. Our results thoroughly detail changes in gene expression patterns and uncover interactions between stem cells and their microenvironment, demonstrating the unique ability of unbiased spatial profiling methods to reveal the biology of regeneration.

MAIN TEXT

Identifying organizing principles that govern the interactions between stem cells and differentiated cells during formation of the regeneration bud or blastema remains a major outstanding goal in regenerative biology. To characterize tissue architectures associated with

whole-body regeneration in planaria, we produced spatial gene expression data by placing regenerating tissue fragments on a “puck” of uniquely identifiable RNA-capturing beads with known locations[8,9]. Planarians were amputated and regenerating tissue assayed at 6 and 48 hours post amputation (hpa). For each time point, tail fragments were arranged around an intact animal and embedded in a block of OCT medium for cryo-sectioning and sample processing (Fig. 1a). Two consecutive coronal sections from both the 6 and 48 hpa samples were placed onto Slide-seqV2[9] pucks for spatial transcriptomic analysis, and adjacent dorsal sections were stained with H&E or DAPI for imaging of tissue morphology (Fig. 1b). Captured mRNA was sequenced, quality filtered, and mapped back to bead locations in two-dimensional space (Fig. 1c). Importantly, beads under tissue generated more UMI counts than those not under tissue, facilitating identification of tissue fragments and removal of background bead data without the loss of beads at the edge of tissues (Extended Data Fig. 1). Moreover, anterior-posterior axes of each fragment could be annotated manually, allowing reorientation into a spatial embedding that grouped them by time point and by adjacent tissue section (Fig. 1d).

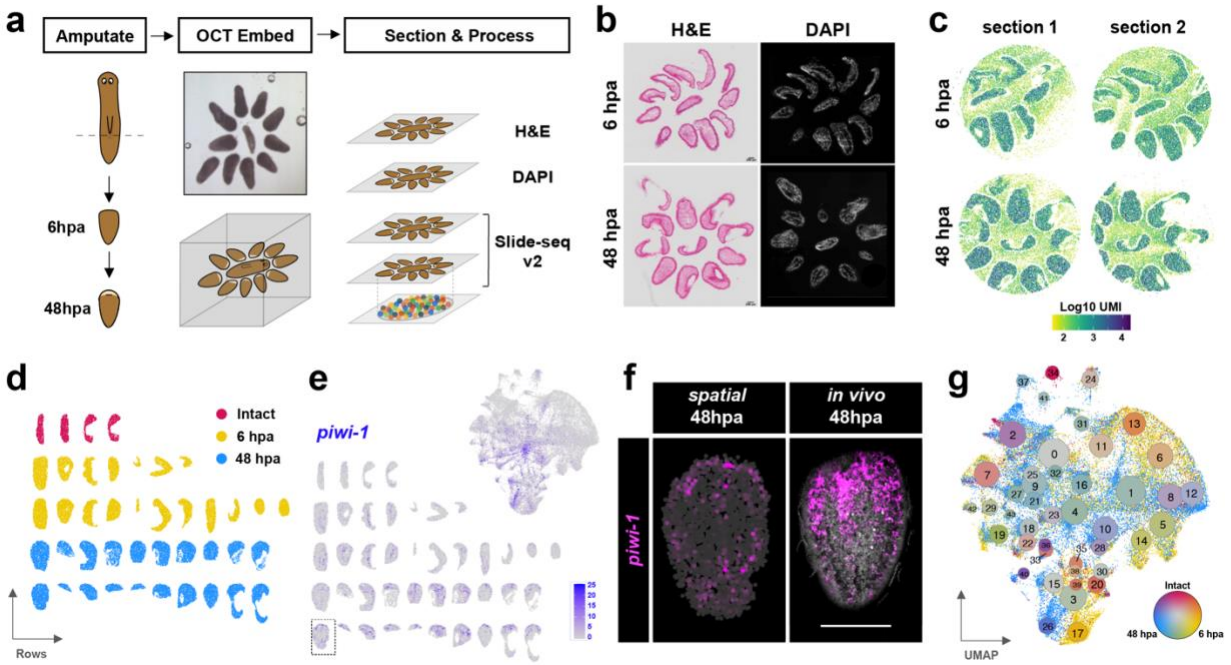

Fig.1: A spatial atlas of regeneration in planarians.
a, Diagram of experiment. Approximately 10 regenerating planarian tail fragments at both 6 and 48 hpa were co-embedded around a single intact planarian and sectioned for Slide-seq. Two adjacent sections were analyzed on separate pucks. Two additional sections were stained and imaged. **b,** Images of adjacent sections from both timepoints stained with H&E or DAPI. **c,** spatial visualization of UMI counts on pucks. **d,** “Row-embedding” of beads under the regenerating tissue fragments. Colors indicate timepoint of origin. Fragments have been rotated to face anterior poles face upward. **e,** UMAP representation of 44 clusters generated from the data. Clusters are labeled with circles proportional in area to the number of beads and colored by relative proportion of beads from each timepoint. **f,** UMI counts detected for the stem cell marker *piwi-1* are overlaid on row-embedding and UMAP plots. **g,** Comparison of *piwi-1* expression revealed by fluorescent *in situ* hybridization and spatial UMI counts at 48 hpa. Scale bar = 500 microns.

Beads under tissue were computationally clustered and embedded in UMAP space (Extended Data Fig. 1)[12,13]. To investigate tissues that may have contributed to each bead cluster, we used Seurat's label transfer functionality to assign relative tissue expression weights to each bead based on a published single cell RNA-seq (scRNA-seq) dataset[3] (). We then determined average tissue expression weights for each cluster (Extended Data Fig. 2a)[12]. In addition, gene markers of each bead cluster were identified. Predicted spatial expression patterns of known tissue markers[3] were compared to *in vivo* expression patterns (Extended Data Fig. 2). Overall, we observed strong correlation between predicted expression in the spatial dataset and *in vivo* expression patterns. *Piwi-1* is the primary marker gene used to identify planarian stem cells and is one of the most abundant transcripts in that cell type[14]. Our spatial transcriptomic data for individual fragments recapitulated the *in vivo* expression pattern of *piwi-1*$^+$ stem cells, including their accumulation close to the wound site at 48 hpa (Fig. 1e, f)[1,15]. This indicates that our dataset accurately captured tissue architecture in regenerating planaria. Finally, for each bead cluster, the relative fraction of beads derived from each timepoint was calculated and presented using a single color (Fig. 1g). Notably, several bead clusters were heavily biased towards a single time point. For example, clusters 17 and 26 occupied adjacent positions in UMAP space but were nearly specific to the 6 hpa or 48 hpa sample, respectively. Therefore, some transcriptional states captured in 2-dimensional space were specific to early or late wound responses.

Since we captured wound-responsive transcriptional states, we next sought to identify which bead clusters were enriched near the wound site. We created a statistical metric to quantify the distribution of each captured bead cluster relative to the wound site, which we termed "Anterior distance" ("A-distance"). A-distance is defined as the distance parallel to the A-P axis to the most anterior bead of a given fragment (Fig. 2a). A-distances were measured for every bead in a cluster at both 6 and 48 hpa (Fig.2b), then averaged for all beads in that cluster at each timepoint (Fig. 2c). This analysis identified clusters that moved closer to the wound through time (Fig. 2c, inset 1) and wound-adjacent clusters (Fig. 2c, inset 2). Notably, two of the wound-adjacent clusters, clusters 17 and 26, were previously identified as temporally biased (Figs. 1g, 2c).

To validate our A-distance predictions, we used *in situ* hybridization to visualize expression of cluster marker genes relative to the wound site. Two clusters which appeared at different spatial positions at 6 hpa and 48 hpa were clusters 4 and 9 (Fig. 2c, Inset 1). Cluster 4 was identified as having reduced A-distance at 48 hpa. It was marked by the stem cell gene *piwi-1* and included beads present in the interior of the body and near the wound at 48 hpa (Fig. 2d, e). *Piwi-1* gene expression *in vivo* mirrored the accumulation of *piwi-1* at the wound site captured in the spatial dataset (Fig. 2e). Fluorescence intensity measurements also confirmed anterior biased expression of *piwi-1* at 48 hpa relative to 6 hpa (Fig. 2f). Cluster 9 included beads mostly located at the lateral edges of the fragments and was marked by the epidermal precursor gene *agat-1* (Fig. 2g, h). *Agat-1* is also a marker of an epidermal Transient Regeneration Activating Cell State (TRACS) known to play a functional role in promoting regeneration[3]. *In situ* hybridization of *agat-1* mirrored the peripheral expression pattern seen in the spatial atlas at both timepoints and characterized a new wound-induced expression domain at the wound site (Fig. 2h). Measurement of fluorescence intensity across the A-P axis of the animal identified anterior biased expression of *agat-1* at 48 hpa relative to 6 hpa, paralleling the reduction in A-distance of cluster 9 in the Slide-seq dataset (Fig. 2i). The analysis of bead clusters 4 and 9 confirmed that a spatial metric ("A-distance"), could be used to identify cellular states that emerge near the wound over time.

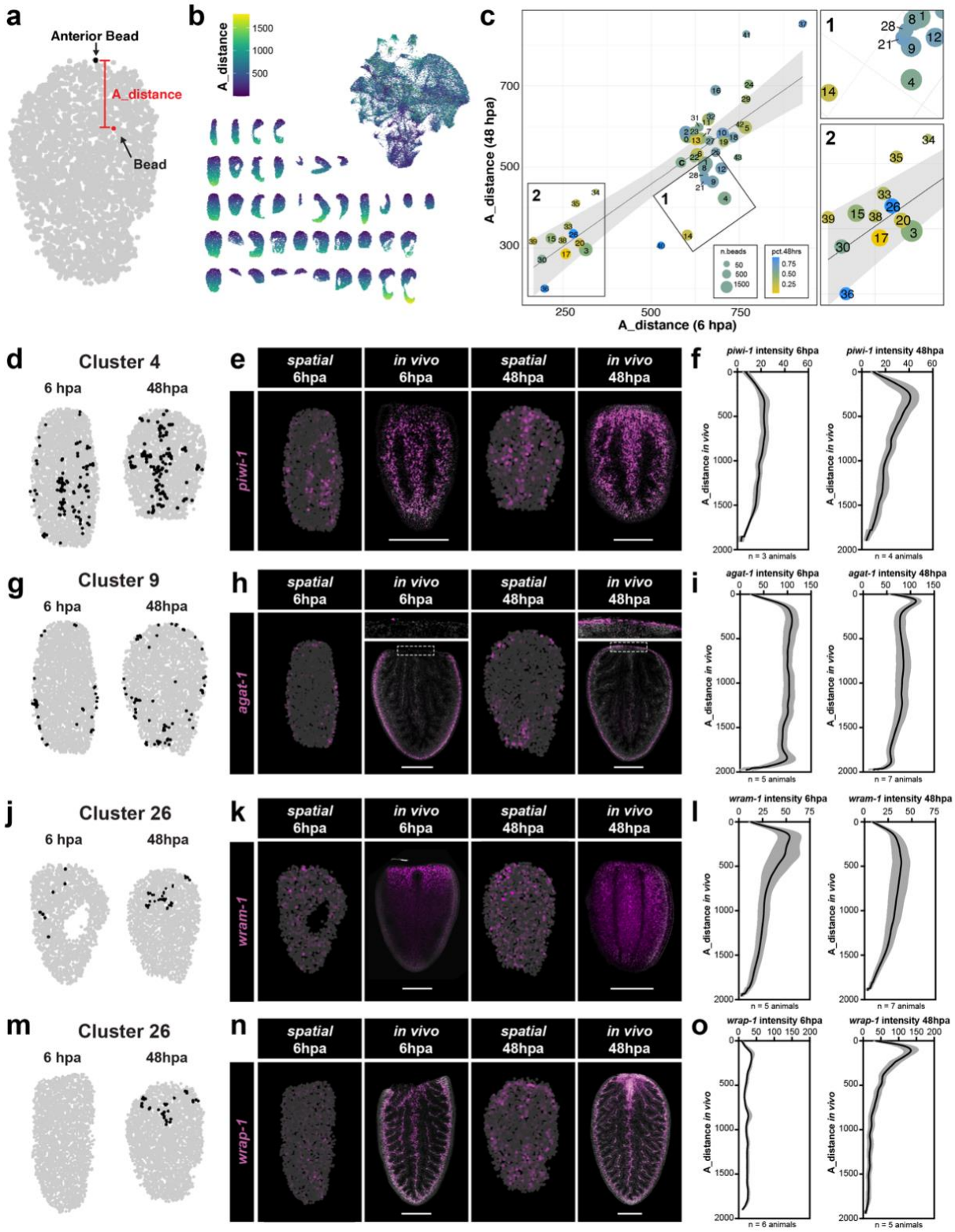

Fig. 2: Identification of transcriptional signatures spatially related to wounding. **a,** Diagram of A-distance calculation. **b,** A-distance visualized on regenerating fragments and UMAP clustering of beads. **c,** Scatterplot of A-distance for Slide-seq clusters at 6 hpa (x-axis)

vs. 48 hpa (y-axis). Data points represent average values for each cluster. Point size represents number of beads in cluster, point color represents fraction of beads from 6 hpa or 48 hpa datasets. **d-o,** Comparison of spatial transcriptomic data to *in situ* hybridization (ISH) signal of marker genes. Beads from clusters of interest are shown in their spatial contexts **(d,g,j,m)**. Visualization of spatial UMI counts for marker genes at 6 hpa, ISH at 6 hpa, spatial UMI counts at 48 hpa, and ISH at 48 hpa **(e,h,k,n)**. Fluorescence intensity as a function of A-distance **(f,i,l,o)**. n = 3 (6 hpa), n = 4 (48 hpa) $P < 2.2 \times 10^{-16}$ (*piwi-1*) **(f)**. n = 5 (6 hpa), n = 7 (48 hpa) $P < 2.2 \times 10^{-16}$ (*agat-1*) **(i)**. n = 5 (6 hpa), n = 7 (48 hpa) $P = 5.44 \times 10^{-15}$ (*wram-1*) **(l)**. n = 6 (6 hpa), n = 5 (48 hpa) $P < 2.2 \times 10^{-16}$ (*wrap-1*) **(o)**. Data are average fluorescence intensity values +/- SEM. Significance assessed using Kolmogorov-Smirnov test. Scale bars = 500 microns.

We next turned to clusters 17 and 26, which are near the wound and occupied by beads mostly from 6 hpa or 48 hpa, respectively. Analysis of genes enriched in clusters 17 and 26 identified several genes predominantly expressed in parenchymal cells, including several matrix metalloproteinases. *In situ* hybridization against matrix metalloproteinase 1 (*mmp-1*), a marker of both clusters, revealed an apparent parenchymal cell population present close to the wound at both 6 and 48 hours post amputation (Extended Data Fig. 3). What distinguished cluster 26 from cluster 17 was enrichment of well-established muscle and stem cell markers, including *collagen* and *piwi-1* (Extended Data Fig. 3)[14,16]. In addition, we identified two uncharacterized genes, SMED30027141 and SMED30005171, also enriched in cluster 26. *In situ* hybridization of SMED30027141 revealed a wound-responsive expression pattern with more anterior expression at 6 hpa than 48 hpa (Fig. 2k,l). Given the enrichment of SMED30027141 in muscle tissues in scRNAseq datasets[17,18] and in wound-induced muscle TRACS[3], we named this gene Wound-Responsive Associated with Muscle-1 or *wram-1. In situ* hybridization of SMED30005171 at 6 and 48 hpa revealed a stem cell-like expression pattern and recapitulated the wound-adjacent A-distance distribution at 48 hpa detected by the spatial atlas (Fig. 2n, o). Given co-expression with *piwi* genes in scRNAseq datasets[3,17,18], we named this gene Wound-Responsive Associated with *Piwi* or *wrap-1*. Overall, beads in cluster 17 captured a relatively pure parenchymal cell transcriptional signature, while beads in cluster 26 captured a blend of parenchymal transcripts with wound-induced muscle and stem cell transcripts. Based on this data, we hypothesized that beads in our dataset may have captured information about cell-cell interactions during regeneration.

Two possibilities could explain how beads in cluster 26 captured both parenchymal and stem cell transcripts. Cells at 48 hpa could express genes that normally mark different populations of cells in intact animals. Alternatively, stem cells and parenchymal cells might be located closer to one another at the 48 hpa timepoint, allowing co-deposition of mRNA from both to be captured on the same beads. To distinguish between these two possibilities, we performed double fluorescent *in situ* hybridization with *mmp-1* and *piwi-1*. Confocal imaging revealed that *mmp-1* and *piwi-1* are expressed in mutually exclusive cell populations, ruling out co-expression in the same cells (Fig. 3a). Three-dimensional rendering of high-magnification confocal images was used to reveal more detail, showing that *mmp-1*$^{+}$ cells are surrounded by much greater numbers of *piwi-1*$^{+}$ stem cells at 48 hpa (Supplementary Video 1). This supports the idea that closer proximity between these cell types following amputation allowed mRNA from both cell populations to be deposited on the same beads. To confirm this result, we visualized *mmp-1* and *piwi-1* using the alternative chemistry of the Hybridization Chain Reaction (HCRv3)[19]. Again, high-magnification confocal images revealed that *mmp-1* and *piwi-1* were not expressed in the same cells, but that separate cells expressing these markers could be found in close spatial proximity at 48 hpa (Fig. 3b). To test our co-deposition model, we quantitated HCR signals of these two markers within areas simulating the capture regions of individual Slide-seq beads. Circles measuring 15 microns in diameter were tiled across images from both timepoints to represent 10 micron Slide-seq beads capturing molecules from their surrounding vicinity (Fig.

3c). At each timepoint, circles greater than or equal to 0.3 of maximum fluorescence intensity were designated as *mmp-1*$^{+}$ (Fig3. d,e). The *piwi-1* fluorescence intensity within these *mmp-1*$^{+}$ circles was twice as high at 48 hpa relative to 6 hpa (Fig. 3f). Together these data support the model that *mmp-1*$^{+}$/*piwi-1*$^{+}$ bead clusters detected in the spatial atlas reflect a closer physical association of parenchymal cells and stem cells during regeneration.

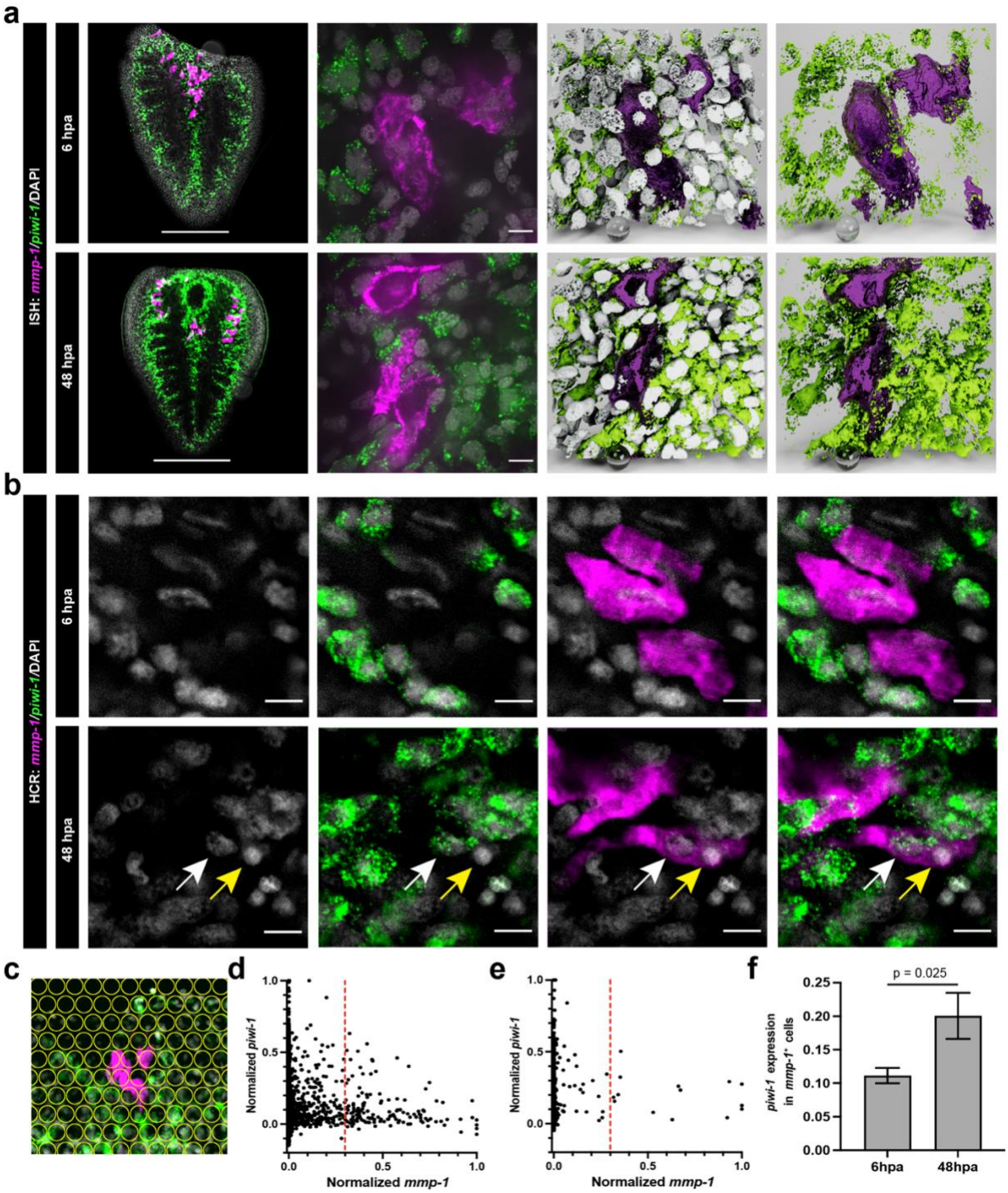

Fig. 3: Regeneration promotes the spatial association of *piwi-1*-positive and *mmp-1*-positive cells. a, Left: Fluorescent in situ hybridization of *mmp-1* (magenta) and *piwi-1* (green) with DAPI staining of nuclei (white). Scale bars are 500 microns for whole-mount sections and 10 microns for tissue sections. Right: 3-D reconstructions of *in situ* images with 10 micron scale sphere. See Supplementary Video 1 for further detail. **b,** Hybridization chain reaction (HCR) of *mmp-1* (magenta) and *piwi-1* (green) with DAPI staining of nuclei (white). White arrows indicate nucleus of *piwi-1*$^+$ cell, yellow arrows indicate nucleus of *mmp-1*$^+$ cell. **c,** HCR images were divided into circular regions 15 microns in diameter. **d,e,** Integrated density of fluorescence in circular regions at 6 hpa **(d)**, or 48 hpa **(e)**. **f,** Data are mean *piwi-1* fluorescence +/- SEM in *mmp-1*$^+$ circular regions. Significance was assessed using unpaired two-tailed Student's t-test. n = 138 (6 hpa) and 14 (48 hpa) regions of interest obtained from analyzing three animals from each time point.

It is possible that enrichment of stem cells near parenchymal cells is due to general accumulation of stem cells near the wound site. To better understand the specificity of the spatial interaction between stem cells and other cell types during regeneration, we calculated "delta-*piwi*" for each bead cluster in the dataset. Delta-*piwi* is defined as the change in the average amount of *piwi-1* expression between the 48 hpa beads and 6 hpa beads within a bead cluster. Thus, clusters with a high delta-*piwi* represent transcriptional environments captured in the dataset with increasing stem cell signatures after amputation. We visualized the results on a global UMAP embedding of the spatial dataset and found that the clusters with the largest increases in *piwi-1* values were closely associated with each other in UMAP space, indicating related transcriptional signatures (Fig. 4a). Expression analysis of known tissue markers revealed that high delta-*piwi* strongly correlated with a parenchymal tissue signature. Moreover, this was true not only for cluster 26, but many parenchymal bead clusters with low A-distance (Extended Data Fig. 4, inset). To interrogate the relationship between the low A-distance parenchymal clusters, we re-embedded this subset of clusters in UMAP space, revealing various clusters radiating out from the centrally located cluster 17 (Fig. 4b). Visualizing delta-*piwi* on this same UMAP plot highlighted that every cluster except for cluster 17 had a positive delta-*piwi*, reflecting the presence of increased *piwi-1* mRNA at 48 hpa (Fig. 4c). To better understand the molecular differences between these stem cell-associated parenchymal bead clusters, we first compared genes enriched across the parenchymal clusters, identifying unique transcripts for each. The clusters shared primary parenchymal and secondary stem cell signatures, but were distinguished from one another by tertiary signatures that include markers of other differentiated tissues (Extended Data Fig. 5).

We hypothesized that some of the diversity of the parenchymal bead clusters could come from the heterogeneity of the stem cells themselves. We analyzed expression of stem cell progenitor markers known to be expressed in subsets of *piwi-1* cells[20,21]. When plotting delta-*piwi* alongside *piwi-1* expression, *mmp-1* expression, and lineage markers, we see that high delta-*piwi* clusters contain high and distinct levels of lineage markers, even beyond that of the stem cell-like cluster 4 (Fig. 4d, Extended Data Fig. 6). Analysis of an existing scRNA-seq dataset does not find increased co-expression of *mmp-1* with these progenitor markers at 48 hpa[3], so these data may indicate the selective association of differentiating stem cells with *mmp-1*$^+$ parenchymal cells during regeneration. Together, we propose that these data portray a population of transcriptionally stable parenchymal cells that dominate their local environment at 6 hpa, resulting in the relatively pure expression signature of cluster 17. As regeneration progresses, increased physical association of parenchymal cells with differentiating stem cells results in the emergence of many blended transcriptional environments, represented by the low A-distance parenchymal bead clusters.

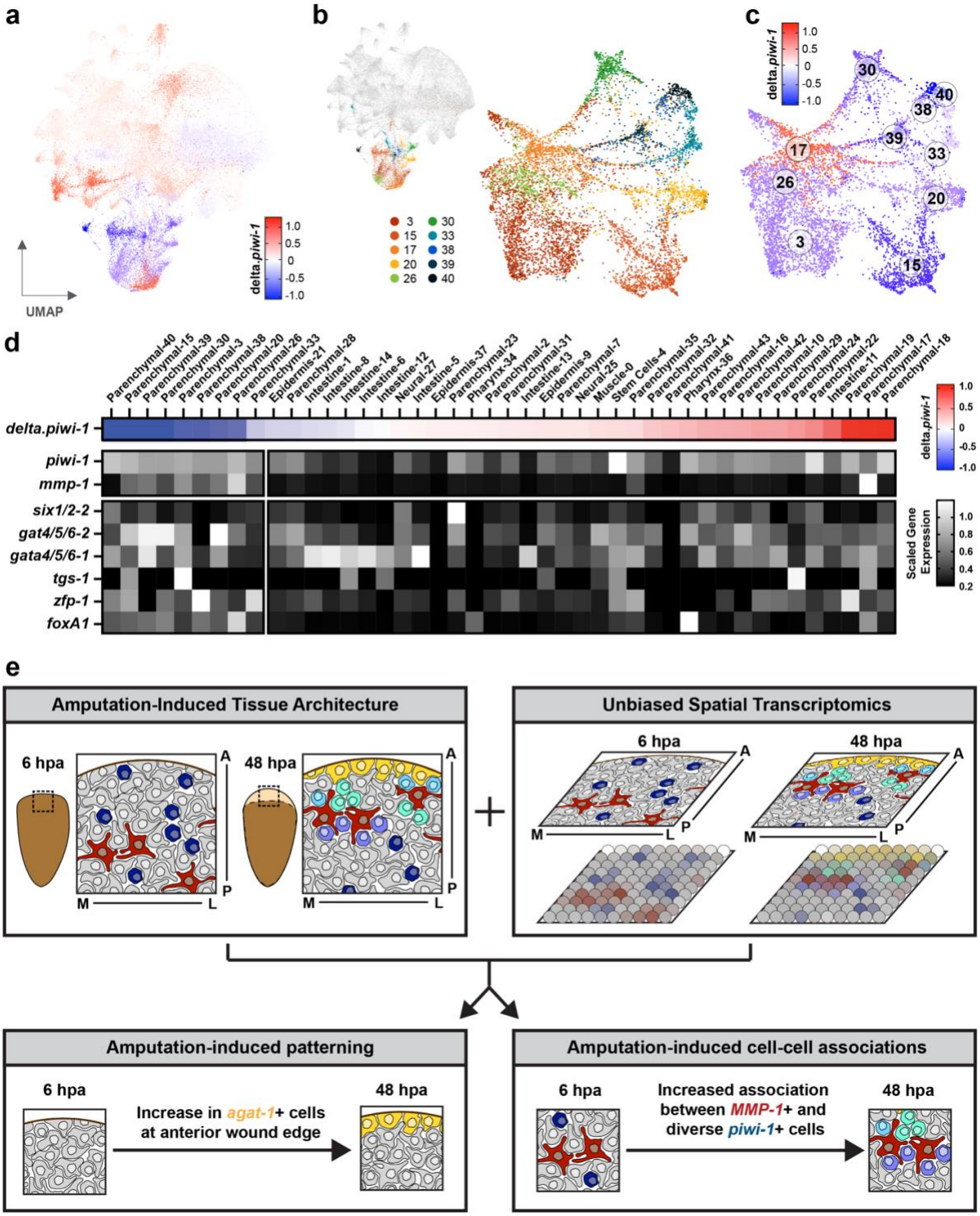

Fig. 4: Differential lineage specification in stem cells distinguishes stem cell-associated parenchymal bead clusters. a, Global UMAP plot of change in average *piwi-1* UMI between timepoints ("delta-*piwi*") for each cluster. **b,** UMAP plots highlighting Low-A-distance parenchymal clusters among global clusters, and Low-A-distance parenchymal clusters reclustered relative to one another. **c,** UMAP plot of reclustered Low-A-distance parenchymal clusters colored by delta-*piwi*. **d,** Heatmaps of average gene expression within Slide-seq

clusters. Top heatmap depicts delta-*piwi-1* for each cluster. Lower heatmaps depict profiles of lineage markers across clusters. Rows are scaled individually to the cluster of maximum expression. **e,** Selected features of regeneration revealed by the dataset. Lower left: new expression domains revealed during regeneration. Lower right:abundant and diverse *piwi-1*$^{+}$ stem cells (blue) accumulate close to the wound site in association with *mmp-1*$^{+}$ parenchymal cells (red).

Our data add spatial context to wound-induced signaling by capturing changes in the cellular organization of regenerating tissue. We used our dataset to characterize two aspects of planarian regeneration: 1) the emergence of new expression domains during regeneration, and 2) increased wound-adjacent associations between parenchymal cells and diverse stem cells, resulting in deposition of their individual RNA molecules onto shared beads (Fig. 4f). Thus, our findings identify both genes and cell types that may play important roles during whole-body regeneration and highlight the types of discoveries spatial transcriptomics can reveal when applied to new research organisms.

DISCUSSION

Single-cell RNA sequencing is a powerful tool that has illuminated the biology of many complex tissues and developmental processes by bringing cell-level analysis to sequencing data[3,17,18,22–25]. Yet, scRNA-seq is blind to how cells are organized in tissues *in vivo*. We used spatial transcriptomics to profile planarian regeneration, bringing near cell-level spatial resolution to RNA sequencing data[8,9]. Our analyses revealed new expression domains of wound-responsive gene expression and a close physical association of *mmp-1*$^{+}$ parenchymal cells with differentiating stem cells in the regeneration blastema.

A-distance calculations (Fig. 2a) facilitated the identification of bead clusters that captured mRNA from wound-responsive cell populations. Validation of the spatial transcriptomic data with *in vivo* marker expression patterns demonstrated the presence of new wound-responsive expression domains at the regeneration blastema. Notably, *agat-1*, a marker of epidermal TRACS, and *wram-1*, a marker of muscle TRACS were identified in this analysis. As these two cell states are required for regeneration[3], our findings demonstrate the power of combining scRNA-seq with spatial transcriptomic approaches to identify cell types and molecules that function during regeneration.

An especially striking facet of our dataset is that beads capturing mRNA from both parenchymal cells and stem cells better distinguish the lineage diversity of the stem cell compartment than do beads that capture mRNA from the stem cells alone. This may indicate that wound-adjacent differentiating stem cells preferentially associate with *mmp-1*$^{+}$ parenchymal cells. The close physical association of *mmp-1*$^{+}$ cells with differentiating stem cells in the blastema may indicate a role for these cell types in regeneration. In other systems, ECM modifying enzymes play important functional roles in regulating stem cell differentiation[26–30]. In planarians, knockdown of *mt-mmpA* produces a small blastema phenotype and recent work has found additional ECM proteins required for successful regeneration[31,32]. Matrix metalloproteinases, which have activity to cleave ECM proteins, could be acting to remodel the ECM, allowing stem cells to mobilize into wound-adjacent tissue and providing them the physical space necessary to grow and proliferate. Additionally, MMP proteins may function biochemically to promote regeneration by liberating proliferation and differentiation factors secreted by nearby tissues. Both physical and biochemical roles for MMP proteins would underscore the importance of modifying the ECM as an initial step in tissue regeneration.

Moreover, the post-mitotic differentiated cells that establish that signaling environment may play a critical role in regulating stem cell differentiation into newly formed regenerating tissues.

Altogether, our work has uncovered unambiguous changes in spatial patterning of gene expression during regeneration and has revealed previously undetected interactions between stem cells and their microenvironment in the blastema. Our results, therefore, demonstrate how unbiased spatial profiling methods can help inform the complex biology driving the restoration of missing body parts.

METHODS

Animal husbandry

Asexual *S. mediterranea* planarians (strain CIW-4 or "C4") were cultured in recirculating culture system as described previously[33]. Tissue biopsies were taken from animals that had been starved for at least one week. Tail fragments were isolated by using 1.25 mm biopsy punches. Fragment size was standardized by positioning the punch over the tip of the animals' tails. The isolated tissue comprised a fragment of roughly the most posterior 1.25 mm tissue of the animal. Small animals used for *in situ* hybridization were starved for at least two weeks prior to use.

Tissue handling and sectioning

Fresh planarian tissue was received in 1x PBS and fragments were embedded together in OCT by timepoint. Tissue fragments were sunk in OCT and arranged in a circle (10-15 fragments oriented closely together with an overall diameter of ~3 mm) around an intact animal. Tissue blocks were then flash frozen at -70°C (HistoChill, Novec™ 7000). After freezing, tissue blocks acclimated to -13°C in a cryostat (Thermo, CryoStar NX70) for 30 minutes prior to sectioning. Tissue blocks were then mounted on a cutting block with OCT and sectioned at a 5° cutting angle with 10 µm section thickness. Pucks were held to clean glass via surface tension (DiH20) and tissue sections mounted directly on each puck. Pucks were then removed from the cryostat and placed into a 1.5 ml Eppendorf tube containing hybridization buffer and prepared for library preparation.

Pre- and post- puck sections were also collected on glass slides for each tissue block sectioned. These sections were air-dried at RT for 20 minutes, fixed in 4% PFA for 15 minutes, and then slides were stained; half the slides with hematoxylin/eosin and half with fluorescent DAPI (1:500). Slides were coverslipped and submitted for imaging. The remaining tissue was wrapped in aluminum foil and returned to −70°C and stored for processing at a later date.

Puck synthesis, library preparation and sequencing

The Slide-seq pucks used in this study were generated and sequenced at the Broad Institute (Cambridge, MA) by Dr. Fei Chen's group according to the methods and supplementary information provided in the *Nature Biotechnology* publication "Highly sensitive spatial transcriptomics at near-cellular resolution with Slide-seqV2"[9].The pucks were received at the Stowers Institute for Medical Research on small glass coverslips in 1.7 mL LoBind tubes at room temperature and were stored in the dark at 4°C. The spatial barcode sequencing file of the pucks were generated via monobase ligation chemistry and provided by Dr. Chen's group to be used for later analysis.

Following mounting, pucks with tissue adhered were immediately immersed in 200 µL of hybridization buffer (6X SSC, 2 unit/µL Lucigen RNase inhibitor) for 27 minutes at room temperature to facilitate the binding of mRNA to the spatially barcoded beads of the puck. First strand synthesis was performed in RT solution (115 µL water, 40 µL 5X Maxima RT buffer, 20 µL 10 mM dNTPs, 5 µL RNase Inhibitor, 10 µL 50 µM Template Switch Oligo, 10 µL Maxima H-

RTase) for 30 minutes at room temperature followed by 1.5 hours at 52℃. After reverse transcription, the tissue was removed by adding 200 µL 2X Tissue Digestion Buffer (100 mM Tris pH 8.0, 200 mM NaCl, 2% SDS, 5 mM EDTA, 32 unit/µL Proteinase K) and incubation at 37℃ for 30 minutes.Following this incubation, 200 µL of Wash Buffer (10 mM Tris pH 8.0, 1 mM EDTA, 0.01% Tween-20) was then added and the mixture pipetted to remove the beads from the coverslip. A series of three washes were performed on the beads using 200 µL Wash Buffer for the first two washes and 200 µL 10 mM Tris-HCl (pH 8.0) for the last wash and by pelleting for 3 minutes at 3000 RCF, removing the supernatant and resuspending. Samples were then treated with exonuclease I solution (170 µL water, 20 µL ExoI buffer, 10 µL ExoI) for 50 minutes at 37°C. A series of two washes were performed on the beads using 200 µL Wash Buffer and pelleting for 3 minutes at 3000 RCF, removing the supernatant and resuspending. Samples were then resuspended in 0.1 N NaOH and incubated for 5 minutes at room temperature followed by a series of two washes in 200 µL Wash Buffer.Beads were resuspended in 200 µL TE, pelleted, supernatant removed and finally resuspended in Second Strand Mix (133 µL water, 40 µL 5X Maxima RT buffer, 20 µL 10 mM dNTPs, 2 µL 1 mM dN-SMRT oligo, 5 µL Klenow Enzyme) and incubated for 1 hour at 37°C. The beads were washed three times with 200 µL Wash Buffer then resuspended with 200 µL water, pelleted for 3 minutes at 3000 RCF and finally resuspended in cDNA PCR mix (88 µL water, 100 µL Terra PCR Direct Buffer, 4 µL Terra Polymerase, 4 µL 100 µM Truseq PCR handle primer, 4 µL 100 µM SMART PCR primer). cDNA was amplified by PCR using the following program:

98°C, 3 minutes
4 cycles of:
    98°C, 20 seconds
    65°C, 45 seconds
    72°C, 3 minutes
9 cycles of:
    98°C, 20 seconds
    67°C, 20 seconds
    72°C, 3 minutes
72°C, 5 minutes
4°C, forever

The PCR product was purified with 0.6X AMPure XP beads (Beckman Coulter, A63881) twice, resuspended in 20 µL water, and checked for quality and quantity using a Bioanalyzer (Agilent) and Qubit Fluorometer (ThermoFisher).

Subsequent library preparation was performed according to manufacturer's directions for the Nextera XT kit (Illumina, FC-131-1096) starting with 600 pg of cDNA and using a specific P5-Truseq PCR hybrid oligo in place of the Nextera XT i5 adapter (15ul Nextera PCR mix, 8 µL water, 1 µL 10 µM P5-Truseq PCR hybrid oligo, 1 µL 10µM Nextera N70X oligo).The resulting short fragment libraries were checked for quality and quantity using the Bioanalyzer (Agilent) and Qubit Fluorometer (ThermoFisher).Sequencing was performed on two High-Output flow cells of an Illumina NextSeq 500 instrument using NextSeq Control Software 2.2.0.4 with the following paired read lengths: 42 bp read 1, 8 bp I7 index, and 42 bp read 2.

Data processing and alignment

Following sequencing, Illumina Primary Analysis version NextSeq RTA 2.4.11 and Secondary Analysis version bcl2fastq2 v2.20 were run to demultiplex reads for all libraries and generate FASTQ files. The sequence data was run through the Slide-seq pipeline[8,9] with default settings. Code was retrieved from the Macosko Lab github page: https://github.com/MacoskoLab/slideseq-tools. Reads were mapped to the Sánchez Alvarado

lab transcriptome[34] and both mapped read 2 data and unmapped read 1 data were processed using Syrah, a Slide-seq pipeline augmentation[35], in order to improve read count and reduce noise, resulting in a single digital gene expression matrix for each puck.

Spatial embeddings

The R package Seurat v 4.0.1[12,13,36,37] was used to import the expression data for each puck and add slide x/y coordinates (the “slide” embedding). Slide position and nUMI was used to determine which beads were under tissue fragments, label each fragment, and manually annotate the A-P axis for each fragment. The data were filtered to remove all beads except those under tissue, the data for all four pucks were combined, and the A-P angles were used to re-orient the fragments with the anterior at the top and the posterior at the bottom, organized into rows based on puck and timepoint (the “rows” embedding).

Initial Analysis

Using the Seurat package in R[12], the data were first normalized with SCTransform and the first 55 principle components were calculated. The PCA data were used to generate a UMAP embedding and to find clusters using FindNeighbors followed by FindClusters with resolution = 1. This resulted in 44 clusters.

Label transfer for tissue annotation

Tissue type data from a recent scRNA-seq dataset[3] were used to annotate the Slide-seq data using Seurat’s FindTransferAnchors using 55 PCs, followed by TransferData[12,13]. The highest tissue label score for each bead was used as that bead’s tissue annotation.

Spatial analysis of gene expression

Using the aligned “rows” embedding, the anterior (A) distance for each bead was calculated as the distance from that bead to the anterior-most bead in the same fragment. We determined which beads were on the edge of fragments by taking the centroid of each bead’s 60 closest neighbors. If the bead’s actual position was further than 30 units from the centroid, it was designated an edge bead. For all edge beads, edge distance was calculated as the distance to the closest edge bead within that same fragment (edge beads have edge distance zero).

Gene cloning and riboprobe synthesis

Gene cloning was performed as previously described[3] and plasmid constructs were transformed into E. coli strain HT115. For riboprobe synthesis, PCR products containing a single T7 promoter were amplified using the plasmid constructs as templates. The primer sequences used are below. In vitro transcription was carried out at 25 µL scale according to the manufacturer’s instructions (Roche). Reaction products were precipitated by adding 80 µL ice cold ethanol, 12.5 µL ammonium acetate (7.5 M), and 2 µL glycogen (19-22 mg/mL, Sigma). Pellets were washed twice with 75% ethanol in water and resuspended in 100 µL deionized formamide (VWR).

PCR primers for riboprobe synthesis

PR244F: GGCCCCAAGGGGTTATGTG
FM46: AGACCGGCAGATCTGATATCA

In situ hybridization

Planarian fragments at relevant timepoints were fixed for single-color fluorescent in situ hybridization (FISH) using the NAC method and in situ hybridization was carried out as reported

previously with the following customizations[38]. DAPI staining was performed at a final concentration of 2 ng/µL in MABT and incubated overnight at 4°C. Samples were cleared overnight in 20% ScaleA2 + DABCO solution and mounted the following day.

For double FISH, samples were fixed using NAFA fixation[39]. Samples were blocked in MABT containing 5% horse serum and 1% Western Blocking Reagent (Roche). *In situ* signals were developed using as previously reported, but with the following customizations. Anti-Fluorescein-POD (Jackson Labs) was applied in block solution at a concentration of 1:3000 overnight at room temperature. FAM tyramides were used to develop fluorescein probes. Peroxidase activity was inhibited using 100 mM sodium azide in PBS (+0.3% Tween-20) for 45 minutes on a shaker at room temperature. After washing > 6 times, Anti-Digoxigenin-POD (Roche) was applied in block solution at a concentration of 1:1000 overnight at room temperature. A second signal was developed for the digoxigenin probes using rhodamine tyramides. DAPI staining was performed at a final concentration of 2 ng/µL in MABT and incubated overnight at 4°C. Samples were cleared overnight in 20% ScaleA2 + DABCO solution and mounted the following day.

Hybridization Chain Reaction (HCR v3)

Whole and amputated planaria were killed with the mucolytic N-acetyl-cysteine (NAC), fixed in paraformaldehyde (PFA), bleached in formamide with hydrogen peroxide and dehydrated via methanol gradient as previously described for *in situ* hybridization[38]. HCR v3 was performed according to the manufacturer's HCR RNA-FISH protocol for samples in solution using probe pairs generated by Molecular Instruments (Molecular Instruments, Los Angeles, CA USA)[19]. DAPI was added during the amplification stage hybridization (#40043 Biotium Freemont, CA USA). Worms were cleared in OptiPrep (#D1556 Sigma-Aldrich, St. Louis, MO USA) and mounted in ProLong Glass Antifade Mountant (P36980 ThermoFisher Scientific Waltham, MA USA). Images were acquired on a spinning disc confocal microscope with sCMOS camera (CSU-W1 Nikon Instruments Melville, NY USA).

Microscopy

Automated imaging was used to capture 10X magnification confocal microscopy images of fluorescent *in situ* hybridizations. Overview images of slides were acquired with a Plan Apochromat Lambda 4X objective lens (N.A. 0.2, 1.735 µm/pixel) and masked using a Fiji macro in a Nikon Elements job. DAPI fluorescence was used to identify planarian fragments. Final images were acquired with a Plan Apochromat Lambda 10X objective lens (N.A. 0.45, 0.78 µm/pixel). Images were batch stitched using Fiji macros (https://github.com/jouyun/smc-macros).

High magnification confocal images of *mmp-1*$^{+}$ cells were acquired with an Orca Flash 4.0 sCMOS 100 fps camera at full resolution on a Nikon Eclipse Ti2 microscope equipped with a Yokogawa CSU W1 10,000 rpm Spinning Disk Confocal with 50 µm pinholes. Samples were illuminated with 405 nm (3.9 mW), 488 nm (8.5 mW), and 561 nm (6.1 mW) lasers (LUNV 6-line Laser Launch) with nominal power measures at the objective focal plane. This spinning disk confocal is equipped with a quad filter for excitation with 405/488/561/640 nm. Emission filters used to acquire this image were 430-480 nm, 507-543 nm, and 579-631 nm. The *mmp-1*$^{+}$ cells near the wound site were identified and used to define upper and lower bounds for confocal imaging. A stack of images was acquired with 0.5 µm step size between each image. A Nikon Plan Apochromat 100X oil objective lens (N.A. 1.49, 0.065 µm/pixel) was used to acquire the image. Selected images were cropped in Fiji and used for 3D rendering.

Image Analysis

"A-distance" values were quantitated as follows: tail sections were selected from multiple rounds of automated 10X imaging on the spinning disc, as described above. A single z-slice

was chosen that corresponds to the main plane of gene localization. First, the tail slice image was rotated to place the wound site in a consistent position. Tail slices were of similar but not identical size. To allow for averaging, images were scaled to the same size. To remove background, a rolling ball background subtraction of 200 pixels was applied, followed by a Gaussian blur of radius 50 pixels. A line profile was drawn starting at the wound site to the end of the tail slice, and a kymograph was obtained averaging over the width of the tail slice. This provided a distribution of intensity of the FISH signal, anterior to posterior. The kymographs for a given FISH probe were averaged to obtain the average A-distance plots. Distributions of fluorescence intensity were compared using the Kolmogorov-Smirnov test.

To estimate from microscopy data what extent of *piwi-1* reads we would expect in beads with a high number *mmp-1* reads, we started with sum projections of HCR data over 10 microns (the estimated thickness of tissue slices placed onto the Slide-seq pucks). A rolling ball background subtraction with a width of 250 pixels was applied. As the intent was to integrate fluorescence signal over circles estimating the size of slide-seq beads, it was necessary to carry out a second background subtraction of average intensity found in regions containing no apparent fluorescence signal. Circular regions of interest were placed onto the image – adjacent circles of diameter 15 microns, each separated by 2 microns (see Fig. 3c). Per circular region of interest, integrated intensity was obtained for *mmp-1* and *piwi-1* FISH signal. As intensity can vary from one image to another, for each individual image analyzed, the maximum *piwi-1* bead intensity and maximum *mmp-1* bead intensity were normalized to a value of 1. Data from multiple images were combined. To compare to the Slide-seq data, it was necessary to set a cutoff in this data for beads that would be considered *mmp-1* positive or *mmp-1* negative. A cutoff of 30% of the maximum *mmp-1* intensity was chosen (see Fig. 3d,e). Normalized *piwi-1* intensity was calculated over these regions of interest and presented as a percentage of maximum piwi intensity (see Fig. 3f). Average *piwi-1* intensity in *mmp-1*$^{+}$ regions of interest was compared using an unpaired two-tailed Student's t-test.

3D rendering of in situ images

3D renderings and movies were made using Fiji 3D Viewer[40,41] with a downsample of 4 and a threshold of 2, 20 and 20 for *mmp-1*, *piwi-1*, and DAPI signal, respectively. Resulting surfaces were exported as wavefront files. Meshes were imported into Blender (BO Community) for still images and movies.

REFERENCES

1. Wenemoser, D., Lapan, S. W., Wilkinson, A. W., Bell, G. W. & Reddien, P. W. A molecular wound response program associated with regeneration initiation in planarians. *Genes Dev* 26, 988–1002 (2012).

2. Zeng, A. *et al.* Prospectively Isolated Tetraspanin+ Neoblasts Are Adult Pluripotent Stem Cells Underlying Planaria Regeneration. *Cell* 173, 1593-1608.e20 (2018).

3. Benham-Pyle, B. W. *et al.* Identification of rare post-mitotic cell states induced by injury and required for whole-body regeneration in Schmidtea mediterranea. *Nat Cell Biol* 23, 939–952 (2021).

4. Tanaka, E. M. & Reddien, P. W. The cellular basis for animal regeneration. *Dev Cell* 21, 172–185 (2011).

5. Ferretti, P. & Géraudie, J. *Cellular and molecular basis of regeneration: from invertebrates to humans*. (1998).

6. Wurtzel, O. *et al.* A Generic and Cell-Type-Specific Wound Response Precedes Regeneration in Planarians. *Dev Cell* 35, 632–645 (2015).

7. Ståhl, P. L. *et al.* Visualization and analysis of gene expression in tissue sections by spatial transcriptomics. *Science* 353, 78–82 (2016).

8. Rodriques, S. G. *et al.* Slide-seq: A scalable technology for measuring genome-wide expression at high spatial resolution. *Science* 363, 1463–1467 (2019).

9. Stickels, R. R. *et al.* Highly sensitive spatial transcriptomics at near-cellular resolution with Slide-seqV2. *Nature Biotechnology* 39, 313–319 (2021).

10. Zhuang, X. Spatially resolved single-cell genomics and transcriptomics by imaging. *Nat Methods* 18, 18–22 (2021).

11. Rao, A., Barkley, D., França, G. S. & Yanai, I. Exploring tissue architecture using spatial transcriptomics. *Nature* 596, 211–220 (2021).

12. Stuart, T. *et al.* Comprehensive Integration of Single-Cell Data. *Cell* 177, 1888-1902.e21 (2019).

13. Hao, Y. *et al.* Integrated analysis of multimodal single-cell data. *Cell* 184, 3573-3587.e29 (2021).

14. Reddien, P. W., Oviedo, N. J., Jennings, J. R., Jenkin, J. C. & Alvarado, A. S. SMEDWI-2 is a PIWI-like protein that regulates planarian stem cells. *Science* 310, 1327–1330 (2005).

15. Wenemoser, D. & Reddien, P. W. Planarian regeneration involves distinct stem cell responses to wounds and tissue absence. *Dev Biol* 344, 979–991 (2010).

16. Witchley, J. N., Mayer, M., Wagner, D. E., Owen, J. H. & Reddien, P. W. Muscle cells provide instructions for planarian regeneration. *Cell Rep* 4, 633–641 (2013).

17. Fincher, C. T., Wurtzel, O., Hoog, T. de, Kravarik, K. M. & Reddien, P. W. Cell type transcriptome atlas for the planarian Schmidtea mediterranea. *Science* 360, eaaq1736 (2018).

18. Plass, M. *et al.* Cell type atlas and lineage tree of a whole complex animal by single-cell transcriptomics. *Science* eaaq1723 (2018) doi:10.1016/j.copbio.2016.03.015.

19. Choi, H. M. T. *et al.* Third-generation in situ hybridization chain reaction: multiplexed, quantitative, sensitive, versatile, robust. *Development* 145, dev165753 (2018).

20. Wolfswinkel, J. C. van, Wagner, D. E. & Reddien, P. W. Single-Cell Analysis Reveals Functionally Distinct Classes within the Planarian Stem Cell Compartment. *Cell Stem Cell* 15, 326–339 (2014).

21. Raz, A. A., Wurtzel, O. & Reddien, P. W. Planarian stem cells specify fate yet retain potency during the cell cycle. *Cell Stem Cell* (2021) doi:10.1016/j.stem.2021.03.021.

22. Gerber, T. *et al.* Single-cell analysis uncovers convergence of cell identities during axolotl limb regeneration. *Science* 362, eaaq0681 (2018).

23. Farrell, J. A. *et al.* Single-cell reconstruction of developmental trajectories during zebrafish embryogenesis. *Science* 360, eaar3131 (2018).

24. Siebert, S. *et al.* Stem cell differentiation trajectories in Hydraresolved at single-cell resolution. *Science* 365, eaav9314 (2019).

25. Schier, A. F. Single-cell biology: beyond the sum of its parts. *Nat Methods* 17, 17–20 (2020).

26. Kazanis, I. *et al.* Quiescence and Activation of Stem and Precursor Cell Populations in the Subependymal Zone of the Mammalian Brain Are Associated with Distinct Cellular and Extracellular Matrix Signals. *J Neurosci* 30, 9771–9781 (2010).

27. Morgner, J. *et al.* Integrin-linked kinase regulates the niche of quiescent epidermal stem cells. *Nat Commun* 6, 8198 (2015).

28. Watt, F. M. & Huck, W. T. S. Role of the extracellular matrix in regulating stem cell fate. *Nat Rev Mol Cell Bio* 14, 467–473 (2013).

29. Gola, A. & Fuchs, E. Environmental control of lineage plasticity and stem cell memory. *Curr Opin Cell Biol* 69, 88–95 (2021).

30. Fuchs, E. & Blau, H. M. Tissue Stem Cells: Architects of Their Niches. *Cell Stem Cell* 27, 532–556 (2020).

31. Isolani, M. E. *et al.* Planarians as a Model to Assess In Vivo the Role of Matrix Metalloproteinase Genes during Homeostasis and Regeneration. *PLoS ONE* 8, e55649 (2013).

32. Sonpho, E. *et al.* Decellularization Enables Characterization and Functional Analysis of Extracellular Matrix in Planarian Regeneration. *Mol Cell Proteomics* 20, 100137 (2021).

33. Arnold, C. P. *et al.* Pathogenic shifts in endogenous microbiota impede tissue regeneration via distinct activation of TAK1/MKK/p38. *Elife* 5, (2016).

34. Tu, K. C. *et al.* Egr-5 is a post-mitotic regulator of planarian epidermal differentiation. *Elife* 4, e10501 (2015).

35. Brewster, C. E., Jr., F. G. M., Benham-Pyle, B. W. & Alvarado, A. S. Syrah, a Slide-seqV2 pipeline augmentation. *BioRxiv* (2022).

36. Butler, A., Hoffman, P., Smibert, P., Papalexi, E. & Satija, R. Integrating single-cell transcriptomic data across different conditions, technologies, and species. *Nature Biotechnology* 36, 411–420 (2018).

37. Satija, R., Farrell, J. A., Gennert, D., Schier, A. F. & Regev, A. Spatial reconstruction of single-cell gene expression data. *Nature Biotechnology* 33, 495–502 (2015).

38. King, R. S. & Newmark, P. A. In situ hybridization protocol for enhanced detection of gene expression in the planarian Schmidtea mediterranea. *BMC Dev. Biol.* 13, 8 (2013).

39. Guerrero-Hernández, C., Doddihal, V., Mann, F. G. & Alvarado, A. S. A powerful and versatile new fixation protocol for immunohistology and in situ hybridization that preserves delicate tissues in planaria. *Biorxiv* 2021.11.01.466817 (2021) doi:10.1101/2021.11.01.466817.

40. Schindelin, J. *et al.* Fiji: an open-source platform for biological-image analysis. *Nat Methods* 9, 676–682 (2012).

41. Schmid, B., Schindelin, J., Cardona, A., Longair, M. & Heisenberg, M. A high-level 3D visualization API for Java and ImageJ. *Bmc Bioinformatics* 11, 274 (2010).

ACKNOWLEDGEMENTS

We thank Fei Chen and Evan Murray for providing spatially barcoded pucks and experimental support, the Stowers Planaria Core for support with animal husbandry, Yongfu Wang for assistance with tissue sectioning, Michael Peterson for assistance with Illumina sequencing, Madelaine Gogol and Hua Li for bioinformatic support, Jay Unruh, Sean McKinney, and members of the Sánchez Alvarado lab for helpful discussions and feedback. A.S.A. is an investigator of the Howard Hughes Medical Institute (HHMI) and the Stowers Institute for Medical Research. B.W.B.-P was a Jane Coffin Childs Memorial Fund Postdoctoral Fellow. F.G.M. is a HHMI Postdoctoral Fellow. This work was supported in part by NIH R37GM057260 to A.S.A.

AUTHOR CONTRIBUTIONS

B.W.B.-P. and F.G.M. designed the experiment. B.W.B.-P., F.G.M., S.M., and J.A.M. created tissue sections for analysis. K.E.H. and A.P. performed library preparation and sequencing. B.W.B.-P., F.G.M., C.E.B., E.R.D., S.C., B.D.S. and A.S.A. analyzed the data. B.W.B.-P., F.G.M., E.R.D., and L.E.M. performed and imaged *in situ* hybridizations. C.G.H. optimized *in situ* hybridizations on regenerating planarians. J.A.M. performed and imaged hybridization chain reactions. S.H.N. rendered light microscopy data into three-dimensional models.

ETHICS DECLARATIONS

Competing Interests

The authors declare no competing financial interests.

EXTENDED DATA FIGURES

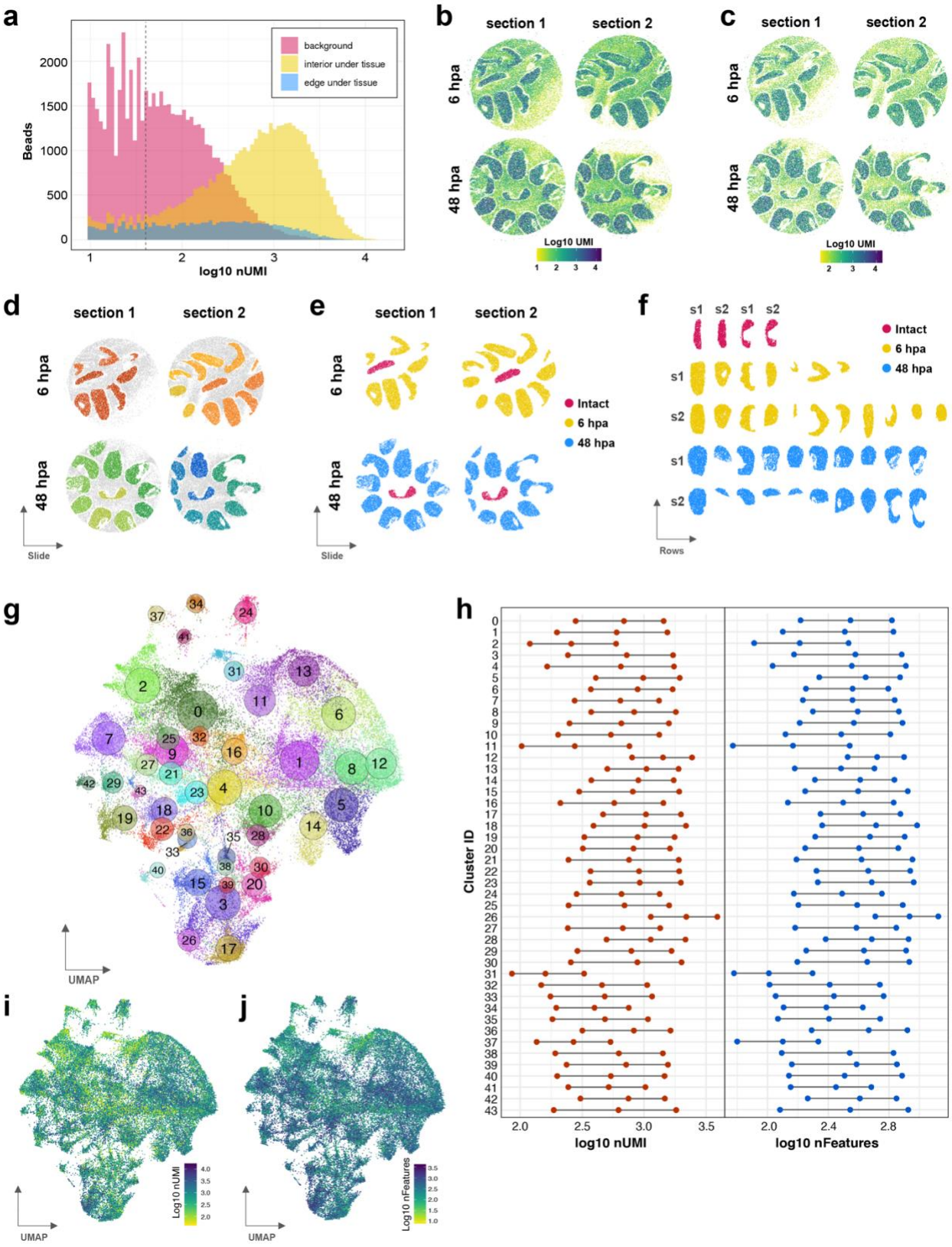

Extended Data Fig. 1: Seurat identifies transcriptional clusters in Slide-seq dataset. **a,** Histogram of UMI counts derived from beads not under tissue (red), under planarian tissue (yellow), or at the edges of fragments (blue). Dotted line at 40 UMI represents cutoff used for subsequent analyses. **b, c,** "Puck embedding" visualization of $\log_{10}$ UMI counts across beads of each puck using Seurat's default cutoff of 10 UMI **(b)** or 40 UMI **(c)**. **d,** Puck embedding after boundaries of individual fragments were manually annotated. **e,** Puck embedding following the exclusion of beads not under tissue. Fragments are colored to represent their timepoints of origin. **f,** "Row embedding" visualization fragments after manual annotation of anterior-posterior axes. Fragments are aligned so that anterior poles are at the top of each fragment. Colors represent timepoints of origin. Except for the top row of intact animals, each row represents a single puck. Fragments are ordered so that serial sections of tissue from the same fragment appear in the same position within both rows for that timepoint. **g,** UMAP plot of global clusters produced by Seurat. **h,** Dumbbell plot of $\log_{10}$ UMI counts (red) and $\log_{10}$ feature counts (blue) for global clusters. UMAP plot of total dataset colored by $\log_{10}$ UMI counts **(i)** or $\log_{10}$ feature counts **(j)**.

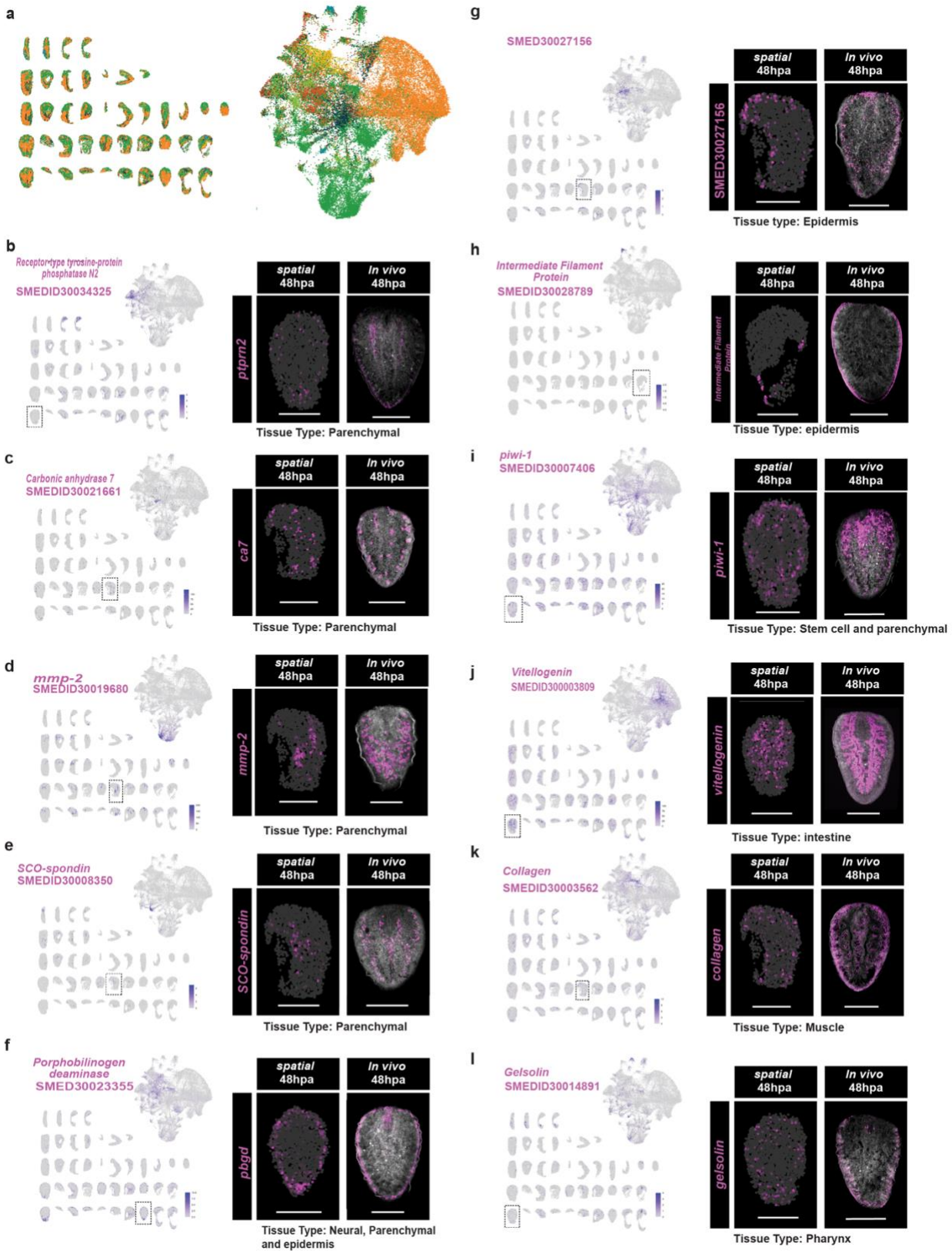
a
b
Receptor-type tyrosine-protein phosphatase N2
SMEDID30034325
ptprn2
spatial 48hpa
In vivo 48hpa
Tissue Type: Parenchymal
c
Carbonic anhydrase 7
SMEDID30021661
ca7
spatial 48hpa
In vivo 48hpa
Tissue Type: Parenchymal
d
mmp-2
SMEDID30019680
mmp-2
spatial 48hpa
In vivo 48hpa
Tissue Type: Parenchymal
e
SCO-spondin
SMEDID30008350
SCO-spondin
spatial 48hpa
In vivo 48hpa
Tissue Type: Parenchymal
f
Porphobilinogen deaminase
SMED30023355
pbgd
spatial 48hpa
In vivo 48hpa
Tissue Type: Neural, Parenchymal and epidermis
g
SMED30027156
SMED30027156
spatial 48hpa
In vivo 48hpa
Tissue type: Epidermis
h
Intermediate Filament Protein
SMEDID30028789
Intermediate Filament Protein
spatial 48hpa
In vivo 48hpa
Tissue Type: epidermis
i
piwi-1
SMEDID30007406
piwi-1
spatial 48hpa
In vivo 48hpa
Tissue Type: Stem cell and parenchymal
j
Vitellogenin
SMEDID300003809
vitellogenin
spatial 48hpa
In vivo 48hpa
Tissue Type: intestine
k
Collagen
SMEDID30003562
collagen
spatial 48hpa
In vivo 48hpa
Tissue Type: Muscle
l
Gelsolin
SMEDID30014891
gelsolin
spatial 48hpa
In vivo 48hpa
Tissue Type: Pharynx

674

Extended Data Fig. 2: Validation of dataset using tissue markers. **a,** Row embedding and UMAP plot colored by major tissue annotation produced by Seurat's Label Transfer function from a previous scRNA-seq dataset[3]. **b, c, d, e, f,** Comparison of Slide-seq data to ISH data for markers of parenchymal bead clusters. Markers shown are: *receptor-type tyrosine-protein phosphatase-N2* **(b)**, *carbonic anhydrase-7* **(c)**, *matrix metalloproteinase-2* **(d)**, *SCO-spondin* **(e)**, *porphobilinogen deaminase* **(f)**. **g,h** Comparison of Slide-seq data to ISH data for markers of epidermal bead clusters. Markers shown: SMED30027156 **(g)**, and *intermediate filament protein* **(h)**. **i, j, k, l,** Comparison of Slide-seq data to ISH data for additional tissues. Tissues/markers shown are: stem cells and parenchyma/*piwi-1* **(i)**, intestine/*vitellogenin* **(j)**, muscle/*collagen* **(k)**, pharynx/*gelsolin* **(l)**. All scale bars = 500 microns.

Extended Data Fig. 3: Marker genes for clusters identified by changes in A-distance and time-bias were validated by ISH. For each gene, the row embedding and global UMAP plot

are shown, along with a comparison of Slide-seq expression data at both 6 hpa and 48 hpa. The genes shown are: *IgGFc-Binding Protein* **(a)**, *lectin-2b* **(b)**, *matrix metalloproteinase-1* **(c)**, *myosin heavy chain* **(d)**, *actin-3* **(e)**, *tubulin alpha-1* chain **(f)**, *DM9 domain-containing protein* **(g)**, *S-adenosylmethionine synthase* **(h)**, *microtubule-actin cross-linking factor-1*, SMED30000059 **(i)**, SMED30014095 **(j)**, *wound-responsive associated with piwi-1* **(k)**. All scale bars = 500 microns.

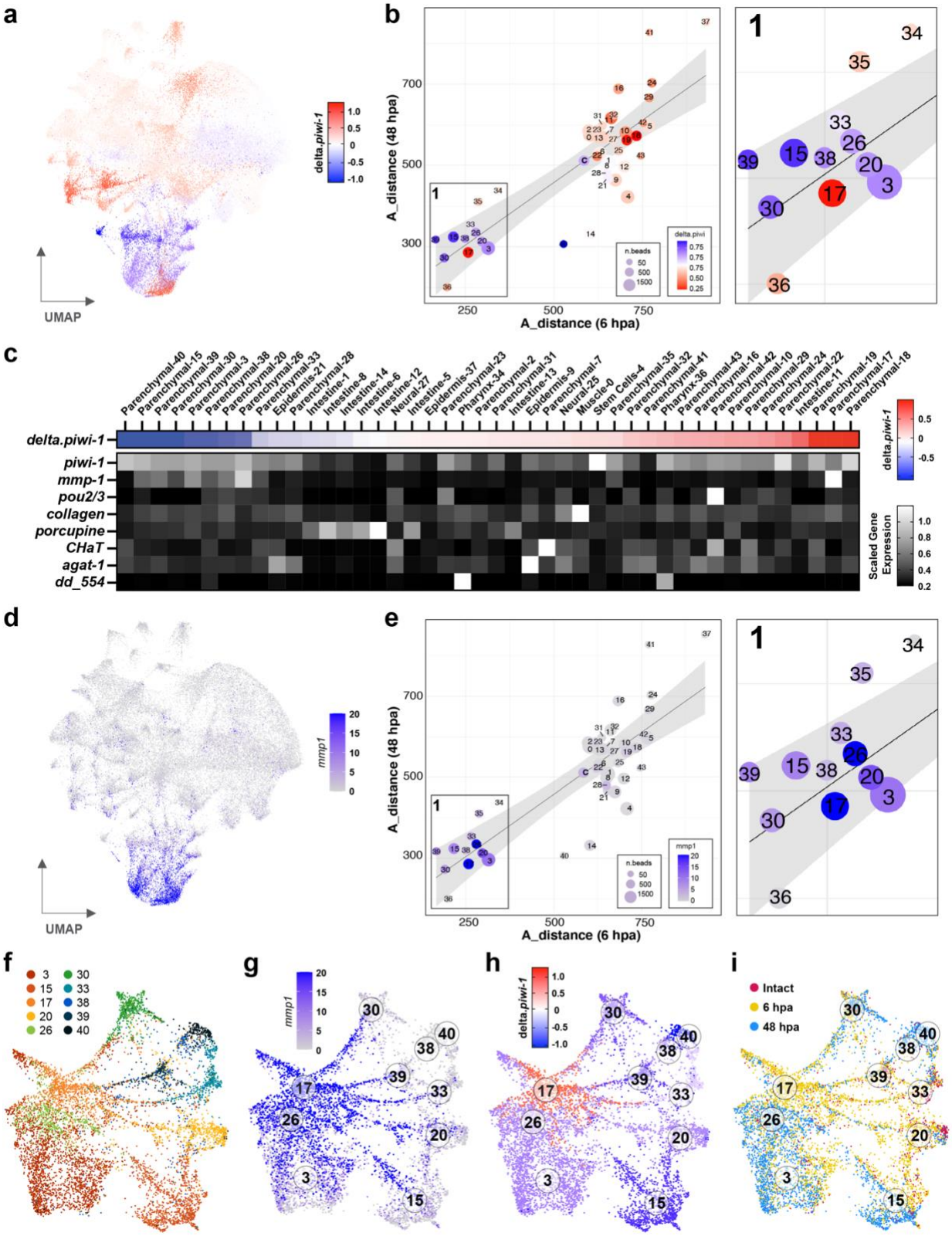

Extended Data Fig. 4: Specialized stem cells associate with *mmp-1*⁺ cells. a, Global UMAP plot of change in average *piwi-1* UMI between timepoints ("delta-*piwi*") for each cluster. Identical

to Fig. 4a. **b,** Scatterplot of average A-distance values for global clusters at 6 hpa vs 48 hpa. Dot area is proportional to the number of beads in the cluster. Dot colors represent delta-*piwi* scores. Inset 1 enlarges “low-A-distance” clusters of interest. **c,** Heatmaps of average gene expression within Slide-seq clusters. Top heatmap depicts delta-*piwi* for each cluster. Lower heatmaps depict profiles of differentiated tissue markers across clusters. Rows are scaled individually to the cluster of maximum expression. **d,** UMAP plot of global clusters colored by *mmp-1* expression. **e,** Scatterplot of average A-distance values for global clusters at 6 hpa vs 48 hpa. Dot colors indicate *mmp-1* expression. Inset 1 enlarges “low-A-distance” clusters of interest. **f, g, h, i,** UMAP plots of Low-A-distance parenchymal clusters relative to one another. Plot is colored to indicate the global cluster of origin (similar to Fig. 4b) **(f)**. Low-A-distance UMAP colored by *mmp-1* expression **(g)**, delta-*piwi* score **(h)**, and timepoint of origin **(i)**.

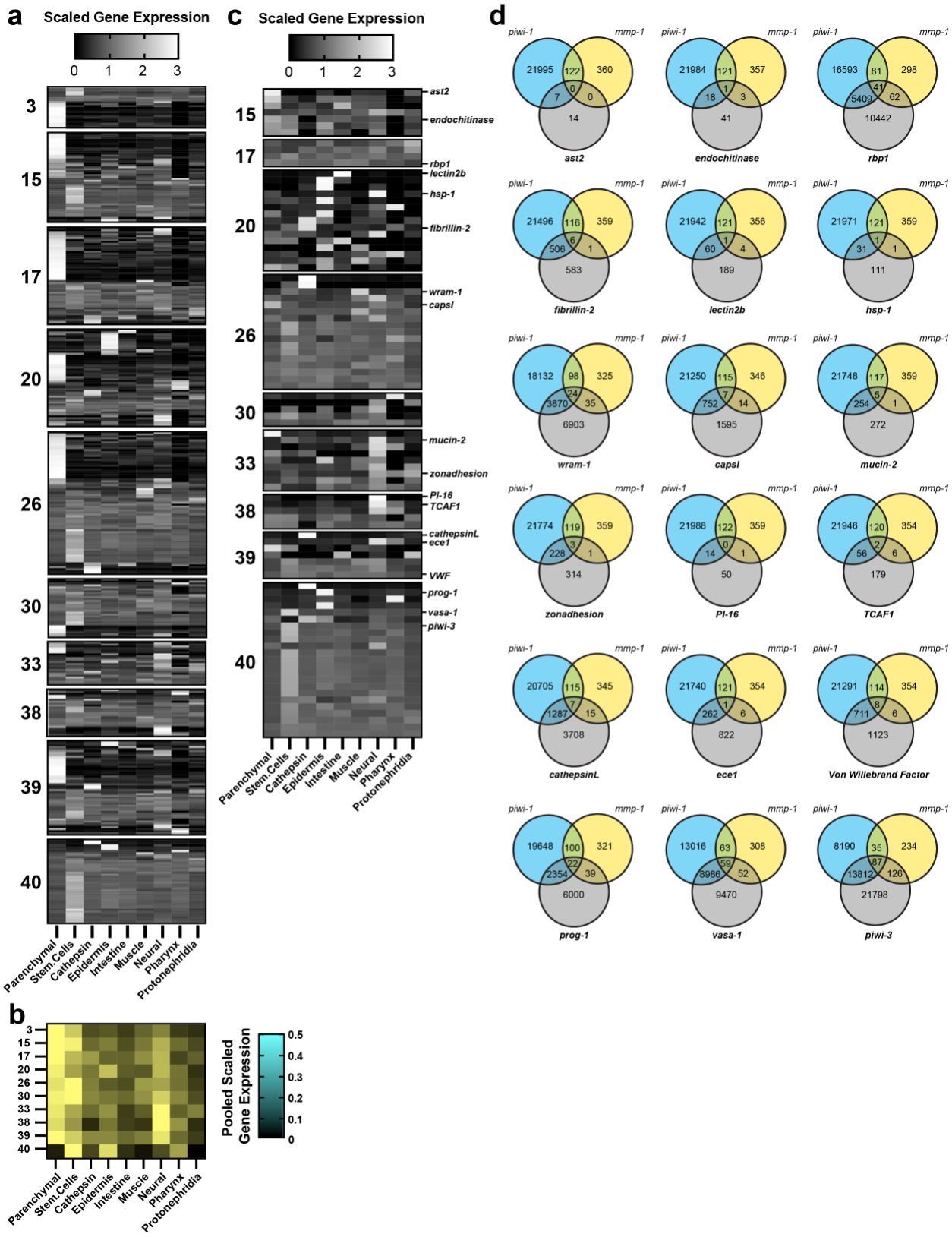
a
Scaled Gene Expression
0 1 2 3
3
15
17
20
26
30
33
38
39
40
Parenchymal
Stem.Cells
Cathepsin
Epidermis
Intestine
Muscle
Neural
Pharynx
Protonephridia
c
Scaled Gene Expression
0 1 2 3
ast2
endochitinase
rbp1
lectin2b
hsp-1
fibrillin-2
wram-1
capsl
mucin-2
zonadhesion
PI-16
TCAF1
cathepsinL
ece1
VWF
prog-1
vasa-1
piwi-3
d
piwi-1
mmp-1
ast2
endochitinase
rbp1
fibrillin-2
lectin2b
hsp-1
wram-1
capsl
mucin-2
zonadhesion
PI-16
TCAF1
cathepsinL
ece1
Von Willebrand Factor
prog-1
vasa-1
piwi-3
b
Pooled Scaled Gene Expression
0.5
0.4
0.3
0.2
0.1
0

Extended Data Fig. 5: Parenchymal clusters are distinguished by associations with other cells. Markers of Low-A-distance parenchymal clusters were analyzed in a published scRNA-seq dataset[3]. Heatmap depicting scRNA-seq expression of a given Slide-seq parenchymal cluster's marker genes **(a)**. Each column represents the average expression across every cell for the given tissue in scRNA-seq. Each row represents a given marker gene from the Slide-seq dataset. Rows are scaled individually. Heatmap depicting average pooled scaled gene expression values across all cells of a tissue **(b)**. Heatmap depicting scRNA-seq expression of the unique marker genes for that parenchymal cluster **(c)**. Rows are scaled individually. Venn diagrams depicting numbers of cells in the scRNA-seq dataset that are positive for *piwi-1*, *mmp-1*, or selected unique markers of parenchymal clusters **(d)**.

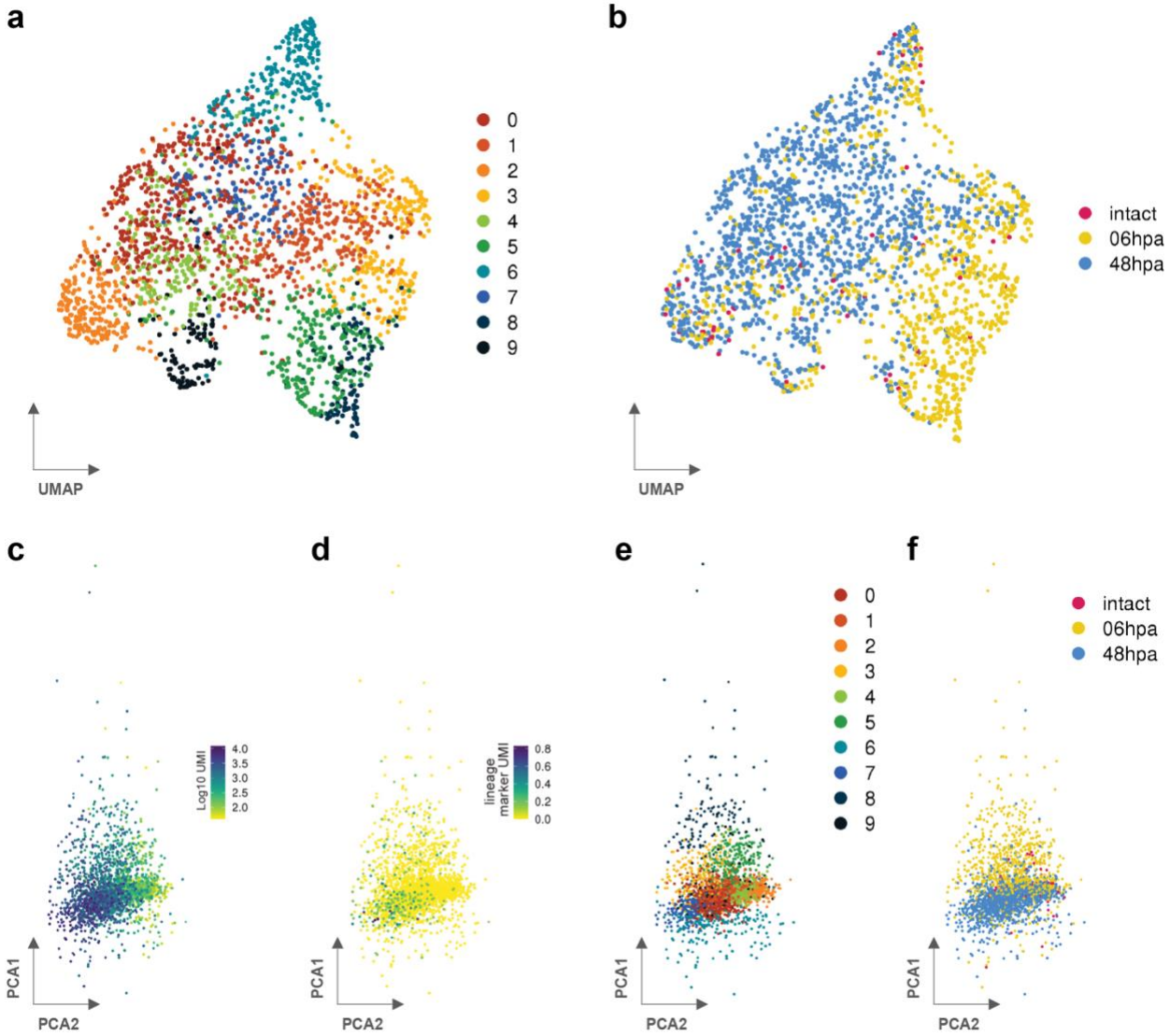

Extended Data Fig. 6: Stem Cell cluster is not a mixture of distinct populations. The subset of beads belonging to cluster 4 – the only cluster annotated as Stem Cells – were analyzed separately and re-clustered. **a,b** UMAP embedding of subset, colored by subcluster **(a)** and timepoint **(b)**. PCA embeddings colored by $\log_{10}$ UMIs **(c)**, mean expression of stem cell lineage markers **(d)**, subcluster **(e)**, and timepoint **(f)**.

SUPPLEMENTARY MATERIALS

Supplementary Video 1: 3D Reconstruction of association between *piwi-1*$^{+}$ and *mmp-1*$^{+}$ cells. Video depicts 3D renderings of fluorescent in situ hybridization of *mmp-1* (magenta) and *piwi-1* (green) with DAPI staining of nuclei (white) from animals 6 hpa (left) and 48 hpa (right). Scale sphere = 10 µm in diameter.